NeuroImage 84 (2014) 206–216

Contents lists available at ScienceDirect

NeuroImage

journal homepage: www.elsevier.com/locate/ynimg

Combined PET/MR imaging in neurology: MR-based attenuation correction implies a strong spatial bias when ignoring bone

Flemming Littrup Andersen [a,*], Claes Nøhr Ladefoged [a], Thomas Beyer [a,b], Sune Høgild Keller [a], Adam Espe Hansen [a], Liselotte Højgaard [a], Andreas Kjær [a], Ian Law [a], Søren Holm [a]

[a] Dept. of Clinical Physiology, Nuclear Medicine and PET, Rigshospitalet, Copenhagen University Hospital, Copenhagen, Denmark
[b] cmi-experts GmbH, CH 8046 Zurich, Switzerland

ARTICLE INFO

Article history:
Accepted 16 August 2013
Available online 29 August 2013

Keywords:
Positron Emission Tomography
PET/MR
Attenuation correction
Neurology
Image reconstruction

ABSTRACT

Aim: Combined PET/MR systems have now become available for clinical use. Given the lack of integrated standard transmission (TX) sources in these systems, attenuation and scatter correction (AC) must be performed using the available MR-images. Since bone tissue cannot easily be accounted for during MR-AC, PET quantification can be biased, in particular, in the vicinity of the skull. Here, we assess PET quantification in PET/MR imaging of patients using phantoms and patient data.

Materials and methods: Nineteen patients referred to our clinic for a PET/CT exam as part of the diagnostic evaluation of suspected dementia were included in our study. The patients were injected with 200 MBq [^{18}F]FDG and imaged with PET/CT and PET/MR in random sequence within 1 h. Both, PET/CT and PET/MR were performed as single-bed acquisitions without contrast administration. PET/CT and PET/MR data were reconstructed following CT-based and MR-based AC, respectively. MR-AC was performed based on: (A) standard Dixon-Water–Fat segmentation (DWFS), (B) DWFS with co-registered and segmented CT bone values superimposed, and (C) with co-registered full CT-based attenuation image. All PET images were reconstructed using AW-OSEM, with neither resolution recovery nor time-of-flight option employed. PET/CT (D) or PET/MR (A–C) images were decay-corrected to the start time of the first examination. PET images following AC were evaluated visually and quantitatively using 10 homeomorphic regions of interest drawn on a transaxial T1w-MR image traversing the central basal ganglia. We report the relative difference (%) of the mean ROI values for (A)–(C) in reference to PET/CT (D).

In a separate phantom experiment a 2 L plastic bottle was layered with approximately 12 mm of Gypsum plaster to mimic skull bone. The phantom was imaged on PET/CT only and standard MR-AC was performed by replacing hyperdense CT attenuation values corresponding to bone (plaster) with attenuation values of water. PET image reconstruction was performed with CT-AC (D) and CT-AC using the modified CT images corresponding to MR-AC using DWFS (A).

Results: PET activity values in patients following MR-AC (A) showed a substantial radial dependency when compared to PET/CT. In all patients cortical PET activity was lower than the activity in the central region of the brain (10–15%). When adding bone attenuation values to standard MR-AC (B and C) the radial gradient of PET activity values was removed.

Further evaluation of PET/MR activity following MR-AC (A) relative to MR-AC (C) using the full CT for attenuation correction showed an underestimation of 25% in the cortical regions and 5–10% in the central regions of the brain. Observations in patients were replicated by observations from the phantom study.

Conclusion: Our phantom and patient data demonstrate a spatially varying bias of the PET activity in PET/MR images of the brain when bone tissue is not accounted for during attenuation correction. This has immediate implications for PET/MR imaging of the brain. Therefore, refinements to existing MR-AC methods or alternative strategies need to be found prior to adopting PET/MR imaging of the brain in clinical routine and research.

© 2013 The Authors. Published by Elsevier Inc. Open access under CC BY license.

Introduction

Dual-modality imaging by means of integrated imaging systems has become a mainstay in clinical routine and research (Beyer et al., 2011). These imaging systems combine Single Photon Emission Tomography (SPECT) or Positron Emission Tomography (PET) with Computed

* Corresponding author at: Dept. of Clinical Physiology, Nuclear Medicine and PET, Rigshospitalet, Blegdamsvej 9, DK-2100 Copenhagen, Denmark. Fax: +45 3545 3898.
E-mail address: fling@pet.rh.dk (F.L. Andersen).

1053-8119 © 2013 The Authors. Published by Elsevier Inc. Open access under CC BY license.
http://dx.doi.org/10.1016/j.neuroimage.2013.08.042

Tomography (CT). Recently, a new combination of PET with Magnetic Resonance Imaging (MRI) has been proposed that offers complementary or even exclusive information compared to PET/CT. All three dual-modality combinations provide anato-metabolic image information (Wahl et al., 1993) that can be used for improved diagnostic assessments and, thus, stratified patient management.

The major advantage of SPECT/CT and PET/CT is the intrinsic alignment of functional and anatomical image information that is acquired in a shorter time than the time needed to perform both examinations independently on separate imaging systems. In addition, the CT images can be used for attenuation correction of the emission data (Kinahan et al., 1998; LaCroix et al., 1994), thus, obviating the need for lengthy, standard transmission scanning using radioactive sources.

However, CT images are limited with respect to soft tissue characterization and tissue contrast. This limits the usefulness of PET/CT, for example, in neurology applications, thus, rendering a separate MRI examination a requirement for many indications. Therefore, combined PET/MR imaging is expected to provide diagnostic information similar or better than that of PET/CT, while soft tissue contrast is improved and patient exposure to ionizing radiation is reduced in PET/MR (Pichler et al., 2010).

Today, two vendors propose somewhat different design concepts for whole-body PET/MR imaging systems. In 2010, Philips Healthcare introduced a sequential PET/MR system combining a time-of-flight (Budinger, 1983) PET together with a 3T MR (Kalemis et al., 2013; Zaidi et al., 2011). In 2012, Siemens Healthcare received FDA approval for a fully-integrated PET/MRI system based on MR-compatible PET detectors mounted inside the MR system (Delso et al., 2011). While no evidence exists today for the clinical superiority of simultaneous PET and MRI acquisitions, it is clear that the simultaneous acquisition will benefit a number of research intentions and applications. For example, brain imaging of neurologic disorders, such as dementia, as well as neuro-oncology applications will draw from the superior soft-tissue contrast of MR together with advanced MRI techniques measuring, e.g., water diffusion or tissue perfusion (Catana et al., 2012; Heiss, 2009).

Despite the advantages of combined PET/MR imaging the adoption of this new modality in clinical routine, and more so in clinical research, is challenged by the need to perform MR-based attenuation correction (MR-AC) (Hofmann et al., 2009). For the brain this impacts not only on basic research-driven applications, such as neuroreceptor kinetic modeling and quantification, but also on the clinical use of PET, including brain tumor imaging, and dementia.

Attenuation correction is a pre-requisite for in-vivo PET quantification (Huang et al., 1979). In PET-only, attenuation and scatter correction (AC, SC) are performed by using measured attenuation coefficients of 511 keV photons derived from images acquired with integrated standard transmission sources (Watson, 1997). In PET/CT, the X-ray transmission source (up to 140 kVp) is used to generate CT images that can be used to calculate maps of attenuation coefficients at 511 keV (Burger et al., 2002; Carney et al., 2006; Kinahan et al., 1998). Attenuation correction based on transmission source imaging is not an option in PET/MR imaging given the lack of rotating transmission sources in the combined system. Instead various approaches have been presented (Bezrukov et al., 2013) to derive subject-specific attenuation information either from an atlas (Hofmann et al., 2009) or from post-acquisition MR image processing (Keereman et al., 2013; Wagenknecht et al., 2013). Commercial PET/MR systems today have a segmentation routine implemented that separates MR images acquired with dedicated sequences either into three tissue classes (air, lung and soft tissue) (Schulz et al., 2011) or four tissue classes (air, lung, fat and soft tissue) (Martinez-Möller et al., 2009). Neither segmentation method does account for bone tissue attenuation, with attenuation values that are higher than those air, lung, fat and water. Ignoring bone during PET attenuation correction is known to cause a distorted and biased distribution of the reconstructed PET activity concentration (Keller

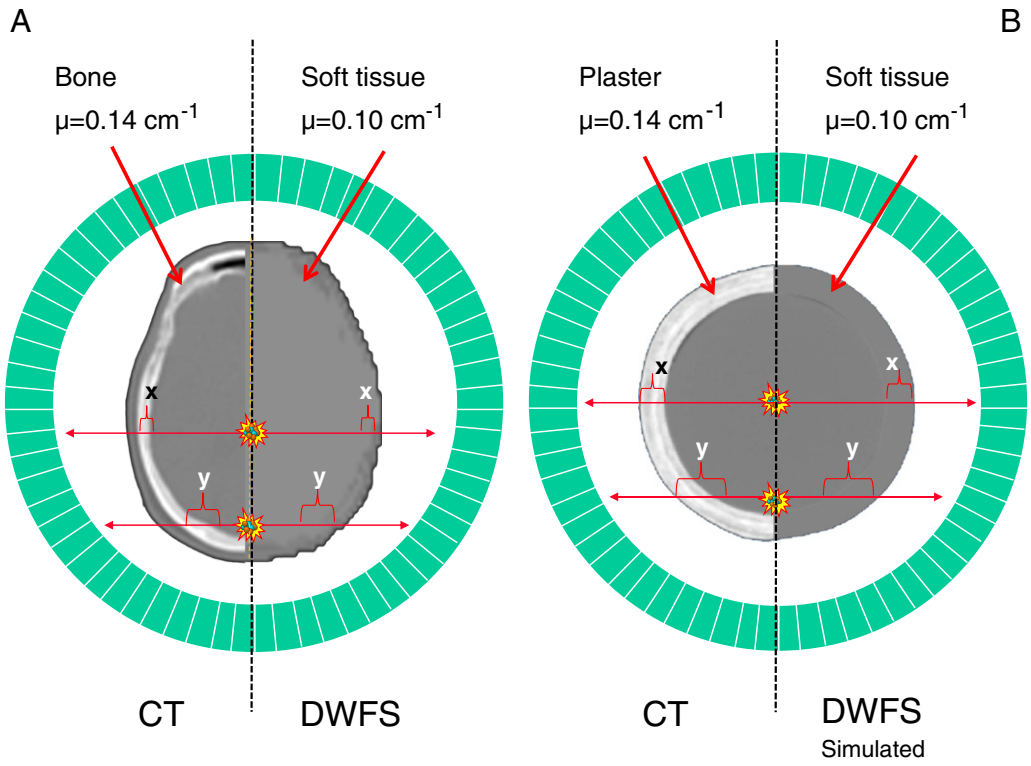

Fig. 1. Explanation of the origin of the bias in reconstructed PET(/MR) tracer distribution in (A) patient and (B) cylinder phantom following MR-based attenuation correction that ignores bone. In both A and B, the left half shows a CT-image while the right part shows the attenuation map from standard MR-AC (acquired in A, simulated in B). The DWFS underestimates the attenuation of the skull as this is replaced by values of soft tissue. The error for a given line-of-response (LOR) depends on the product of the bias of the attenuation coefficient and the length of the path through the skull. Since this path-length is longer for LORs near the edge than for LORs through the center ($y > x$), a bias is introduced in the projections that propagate through reconstruction to the final images resulting in suppression of the edges (cortex).

et al., 2013). This may have particular implications for brain imaging as discussed by Catana et al. (2010).

Fig. 1 illustrates the bias originating from ignoring bone in PET/MR imaging of the brain. The reconstructed voxel value in any point of a PET image is affected by the measured intensity along lines-of-response (LORs) that traverse that voxel. The intensity must be corrected for attenuation prior to reconstructing the emission image. The attenuation correction factor along a given LOR is calculated based on the integral of the tissue attenuation values along that LOR. Fig. 1 shows a cross section of a human head and a cylindrical "skull" phantom. LORs near the edge, traversing the skull at an oblique angle have a longer path through skull bone than central LORs. Therefore, total attenuation along these LORs is affected more by the higher bone attenuation than that of central LORs. Consequently, the overall effect of neglecting bone attenuation is likely to be larger at the edge than at the center, thus, leading to a regionally variable bias.

The purpose of our study was to assess the regional and absolute bias introduced from neglecting bone during MR-AC of combined PET/MR images of the brain. We employ phantom and clinical data from an ongoing commissioning of a fully-integrated, whole-body PET/MRI system.

Materials and methods

Patient studies were performed using a fully-integrated PET/MR system (Biograph mMR, Siemens Healthcare) (Delso et al., 2011) and, for the purpose of reference imaging, on a whole-body PET/CT system (Biograph TruePoint64 or Biograph mCT64, Siemens Healthcare) (Jakoby et al., 2011). All PET systems were normalized using [^{68}Ge]-cylinder phantoms and cross calibrated using a common [^{18}F]-filled phantom. Decay-correction of the PET data from either the PET/CT or the PET/MR examination was always performed to the start time of the first of the two PET examinations.

Based on Fig. 1A a skull-like phantom was prepared (Fig. 1B) to assess the effect of bone in MR-AC. Subsequent findings were tested in patients who were recruited from an ongoing study on the clinical value of PET/MR imaging in dementia.

Phantom study

A 2 L plastic bottle was fitted with a layer of approximately 12 mm non-synthetic plaster (Gypsona, BSN Medical, Hannover, Germany). The plaster ring extended over 10 cm axially in the center of the phantom (Fig. 2A). A total of 50 MBq of [^{18}F]FDG was injected into the phantom and distributed uniformly. The phantom was placed on the bed parallel to the main axis of the PET/CT, and subsequent CT (120 kVp, 380 mAs, 3 mm slices) and emission scanning were performed over the central phantom (1-bed) layered with the plaster. CT images of the phantom (Fig. 2B) demonstrated a mean CT-density of the plaster of (814 ± 65) HU, corresponding to bone attenuation at 511 keV (linear attenuation coefficient: 0.140 cm^{-1}, (Carney et al., 2006)).

PET images of the phantom were reconstructed following CT-based attenuation correction using the original CT images (PET_{CT}), and the CT images with the image values representing plaster above 50 HU being replaced by the attenuation values of brain tissue of 36 HU (PET_{SOFT}). Here the attenuation map resembles that of a standard MR-based attenuation map following the Dixon-Water–Fat-segmentation (DWFS) (Martinez-Möller et al., 2009), that is the standard method in the fully-integrated PET/MR (Delso et al., 2011). PET image reconstruction

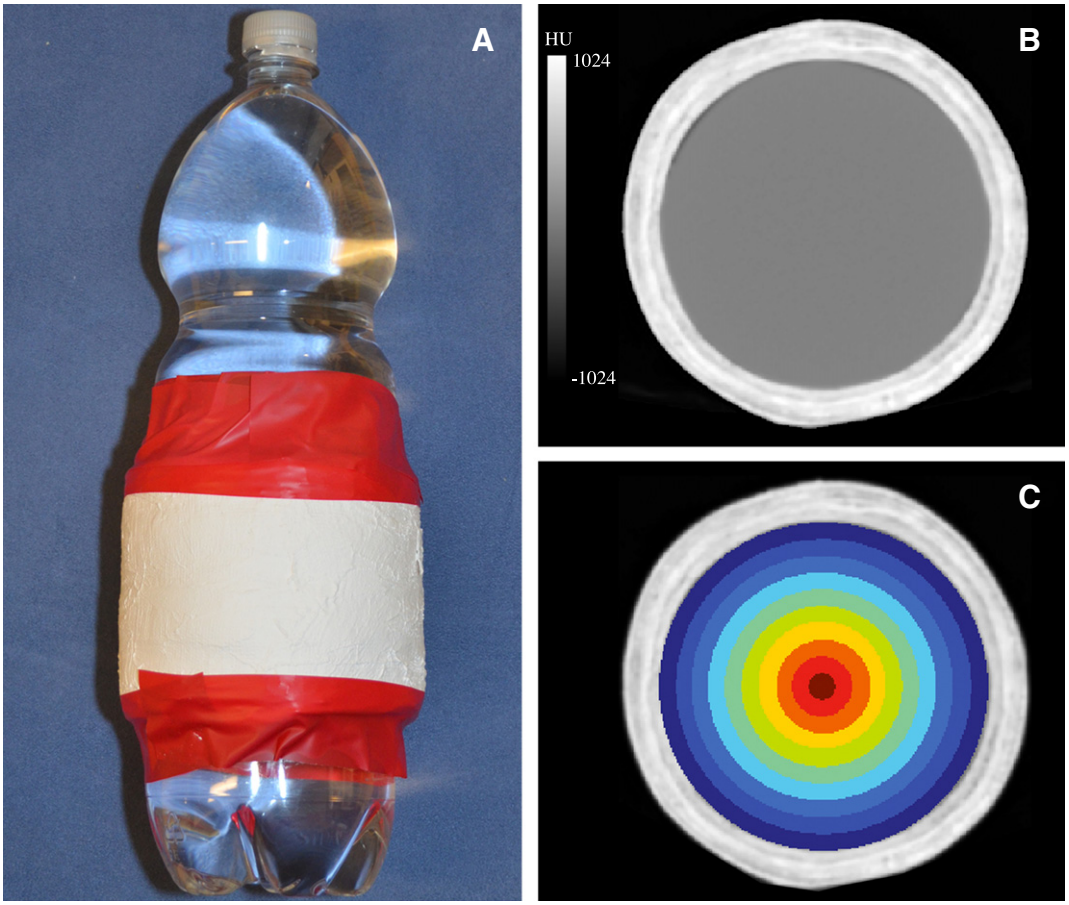

Fig. 2. Skull-like phantom with uniform [^{18}F]FDG activity distribution (25 kBq/mL) inside the mimicked "brain". The "skull" was simulated by a layer of plaster. The high-density "skull" covers 10 cm axially (A); the width of the skull is about 12 mm as seen on the transaxial CT image (B). Concentric annuli of 5 mm width are used to quantify regional changes in the activity concentration from simulated MR-AC.

was performed using the attenuation-weighted ordered subsets expectation maximization (AW-OSEM) (4 iterations 21 subsets, 4 mm Gaussian postfilter) algorithm without resolution modeling and without using time-of-flight (TOF) in order to closely resemble the PET/MR image reconstruction. PET image matrix size was 336 × 336 voxels, with (0.8 × 0.8 × 3) mm voxel size. A 4 mm Gaussian post-reconstruction filter was applied.

The PET images were analyzed using 10 concentric annulus regions of 5 mm width (Fig. 2C) and the mean activity concentrations (kBq/mL) were calculated for all annuli placed over a central transaxial image plane traversing PET_{CT} and PET_{SOFT}. For each annulus, we report the %-differences (Δ%) i.e., $(PET_{SOFT} - PET_{CT}) / PET_{CT}$.

Patient characteristics

19 patients (9 male, 10 female, mean age (68 ± 9) y, range: 43 y–85 y) under evaluation for suspected dementia were referred for an [^{18}F]FDG-PET/CT study and included in this study. Prior approval was obtained from the local Ethics Committee and all patients were able to give informed consent. Patients were injected with 200 MBq of [^{18}F]FDG. Ten patients were imaged on PET/MR first and then on PET/CT while 9 patients were imaged in the reverse order of examinations (Table 1), in an attempt to limit the effects from changes in the tracer uptake and distribution as a function of the post-injection time of the tracer (Krak et al., 2003).

PET/CT acquisition

Patients were positioned head-first supine on the PET/CT with the arms down and the head positioned in the standard head holder attached to the bed. PET/CT imaging was performed at a single PET bed position; with the protocol including a topogram scan, a spiral CT (120 kVp, 36 mAs, 5 mm slice width) and a 10 min 3D-emission scan.

Table 1
Summary of 19 patients referred for an [^{18}F]FDG PET/CT for suspected dementia diagnosis and imaged with PET/CT and PET/MR for a single injection of activity. Patients 1–10 underwent PET/MR imaging first, followed by PET/CT imaging (delay: (66 ± 9) min); patients 11–19 were scanned in reverse order of examinations (intra-scan delay: (46 ± 7) min). M = Male, F = Female.

Subject	Sex	Age (y)	Inj. dose (MBq)	Pi time (min) PET/MR	Pi time (min) PET/CT	Time difference (min)
PET/MR first, followed by PET/CT						
1	M	70	202	35	59	−24
2	F	66	200	41	60	−19
3[a]	M	71	201	41	87	−46
4	F	65	199	32	67	−35
5	M	76	204	43	63	−20
6	M	71	199	43	63	−20
7	F	65	200	38	68	−30
8[a]	M	81	198	46	61	−15
9	F	68	200	45	73	−28
10	F	85	200	40	57	−17
PET/CT first, followed by PET/MR						
11	F	43	205	81	41	40
12[a]	F	70	201	74	45	29
13	M	62	203	97	62	35
14	F	77	201	91	50	41
15	F	71	199	90	45	45
16	M	69	201	83	40	43
17[a]	M	61	196	82	48	34
18	M	54	202	75	46	29
19	F	72	196	69	39	30

[a] Indicates patient with severe artifacts in the MR attenuation map due to dental implants.

PET/CT image reconstruction

PET images from the PET/CT were reconstructed following CT-AC employing the standard bi-linear scaling approach (Carney et al., 2006). PET images were reconstructed using AW-OSEM without resolution modeling and without using TOF, as these options were not available on our PET/MR system at the time of this study. Reconstructed PET images were 336 × 336 matrix size, 4 iterations, 21 subsets and 400 × 400 matrix size, 4 iterations, 24 subsets on the Biograph TruePoint PET/CT and the Biograph mCT, respectively. In all cases a 4 mm Gaussian post-reconstruction filter was applied, and the reconstructed PET voxel size was 0.8 × 0.8 × 3 mm.

PET/MR acquisition

Patients were positioned in the PET/MR in supine position with the arms down. The head was positioned in the head–neck coil. In case the patients were examined on PET/MR first (Table 1, patients 1–10), simultaneous 3D PET/MR imaging of a single PET-bed position was followed by a single-bed PET/CT scan at a mean time interval of (24 ± 9) min. In cases of the PET/MR imaging being performed after the PET/CT examination (Table 1, patients 11–19), the mean time interval between scans was (36 ± 6) min. In each case emission acquisition time was 10 min.

MR imaging included an in-/opposed-phase sequence for Dixon-Water–Fat segmentation (DWFS) (Martinez-Möller et al., 2009) as well as T1w- and T2w-imaging. In- and opposed phase imaging was based on a 3D VIBE-Dixon sequence with a repetition time (TR) of 3.6 ms, echo times (TE's) of 1.23/2.45 ms, a flip angle of 10°, voxel size 4.1 × 2.6 × 3.1 mm^3 and an acquisition time of 19 s. Additional anatomical imaging using T1 was performed as follows: 3D MPRAGE sequence, TR 1900 ms, TE 2.44 ms, flip angle 9°, voxel size 1.0 × 1.0 × 1.0 mm^3 and acquisition time 5 min. Anatomical imaging using T2 was performed as follows: Turbo spin echo (TSE) sequence, TR 6000 ms, TE 96 ms, flip angle 150°, voxel size 0.7 × 0.7 mm^2, slice thickness 4 mm and an acquisition time of 1.25 min. All MR sequences used a parallel imaging factor of 2.

Bone tissue extraction and PET/MR image reconstruction

For each subject, CT images were co-registered to the PET/MR images using a rigid alignment procedure (minctracc, McConell Imaging Center, Montreal). First, the patient bed and head-holder were extracted manually from the CT images using an oval ROI (OsiriX software) applied to each transverse CT image. Subsequently, a CT-based bone representation was defined by masking all CT voxels from the co-registered CT images within the oval ROI with a CT attenuation value of 100 HU, and above. The bone attenuation values were then converted from HU to linear attenuation coefficients at 511 keV by using the standard bi-linear scaling approach (Carney et al., 2006) as implemented in our PET/CT systems.

Three attenuation maps were created. First, the standard MR-based attenuation following DWFS was used, thus, accounting for air, lungs, fat and soft tissue, but not bone (MR_DWFS). Second, the co-registered bone attenuation map was superimposed on the DWFS-map, thus, replacing existing DWFS-based attenuation values with those of bone (MR_Bone). The MR-based attenuation map then accounted for air, lungs, fat, soft tissue and bone. For the third reconstruction, the co-registered standard CT attenuation map replaced the DWFS attenuation map in the volume covered by the CT (MR_FullCT). The three attenuation maps were used for PET/MR reconstruction, resulting in PET_{MR_DWFS}, PET_{MR_Bone} and PET_{MR_FullCT}.

The same PET reconstruction parameters were used for the PET/MR data as for the PET/CT data, with the only change being the matrix size of 344 × 344 and a reconstructed PET voxel size of 0.8 × 0.8 × 2 mm.

PET image analysis

Visual and quantitative analysis was performed of the reconstructed PET images from the PET/CT and the PET/MR examinations using the three approaches to MR-AC. Similar to the phantom study (Fig. 2) we used 10 regions-of-interest (ROI) represented by successive 5 mm deformed annuli that followed the exterior cortical layer and extending from the cortex inwards to the center of the transaxial image plane (Fig. 3). These ROIs were delineated manually on a transaxial T2w-MR image traversing the central basal ganglia. For each patient and image reconstruction the mean FDG activity concentration was calculated for each of the 10 homeomorphic annuli: PET_{CT}, PET_{MR_DWFS}, PET_{MR_Bone}, and PET_{MR_FullCT}.

We report %-differences (Δ%) per annulus and patient for PET_{MR_DWFS} relative to PET_{CT}. We also report Δ% averaged across two groups depending on the scan order of PET/MR and PET/CT for PET_{MR_DWFS}, PET_{MR_Bone} and PET_{MR_FullCT} relative to PET_{CT}. Finally we report %-differences (and standard deviation) for PET_{MR_DWFS} relative to PET_{MR_Bone} and PET_{MR_DWFS} relative to PET_{MR_FullCT} again averaged across all patients. For this analysis, four of the 19 patients had to be excluded since the PET images from the PET/MR were distorted by signal voids arising from susceptibility artifacts caused by dental fillings (Keller et al., 2013).

Results

Phantom study

A significant bias of the reconstructed and attenuation-corrected PET images is found in case bone (plaster) is not accounted for during AC. This is illustrated in Fig. 4 that shows central transaxial image planes through the original and modified CT and PET images using the corresponding attenuation maps. An overall absolute reduction in reconstructed PET activity in case bone is ignored during AC is seen. This is demonstrated when comparing Fig. 4C (PET_{CT}) and Fig. 4D (PET_{SOFT}). The calculated Δ% shows a radial bias that was largest (up to 14%) in the most exterior region representing the cortex and lowest (7%) in the central region of the phantom (Figs. 4E and F).

Clinical PET/MR study

The reconstructed tracer distribution of the phantom study above was replicated in our patient studies. Fig. 5 exemplifies the relative difference of the reconstructed PET activity distribution in patients following standard DWFS MR-AC (PET_{MR_DWFS}) in comparison to PET images following CT-AC (PET_{CT}). The regional variation of the AC-PET distribution in PET_{MR_DWFS} is clearly seen as a volumetric effect with the highest relative difference in the cortical region. In addition, the effect is equally visible on the coronal and sagittal slices, thereby reflecting the "spherical" nature of the skull.

The reconstructed PET activity concentrations in PET/MR images following MR-AC in reference to PET_{CT} for all 19 patients are illustrated in Fig. 6 as the relative difference Δ%(PET_{MR_DWFS}, PET_{CT}). Two distinct observations can be made in this figure. First, an overall sign-inversion, dependent on the scan order due to changes in the physiological tracer uptake between the two scans. Second, a common, gradual decrease of Δ%(PET_{MR_DWFS}, PET_{CT}) is observed from the center to the cortex across all patients, independent of the scan order.

Fig. 7 further exemplifies the visual and quantitative results. For better visual comparison, the PET_{CT} scale is adjusted to that of the PET/MR images to account for the increased physiological uptake of FDG during the intra-scan delay of 17 min. Note, the substantial decrease of reconstructed tracer activity in regions of PET_{MR_DWFS} close to the skull relative to the center (panel I). This effect is largely removed in PET_{MR_Bone} (J) and even further in PET_{MR_FullCT} (K), while residual differences can be attributed to changes of the tracer uptake and distribution during the PET/CT and PET/MR scans. Finally, (L) and (M) show the relative difference of (F, G) in reference to (E), i.e. involving only PET data acquired at one time point on PET/MR.

The visual and quantitative bias as exemplified in the case study in Figs. 5 and 7 is replicated across all subjects (Figs. 8A–C). Note, four of the 19 patients had to be excluded from detailed analysis (Table 1, denoted by "*") due to dental work causing severe MR image artifacts that caused a biased MR-based attenuation map and subsequent artifacts in the reconstructed PET images (Keller et al., 2013).

The gradual radial change of Δ% following MR_DWFS is nicely illustrated in Fig. 8A by averaging over all patients (from Fig. 6). This bias is

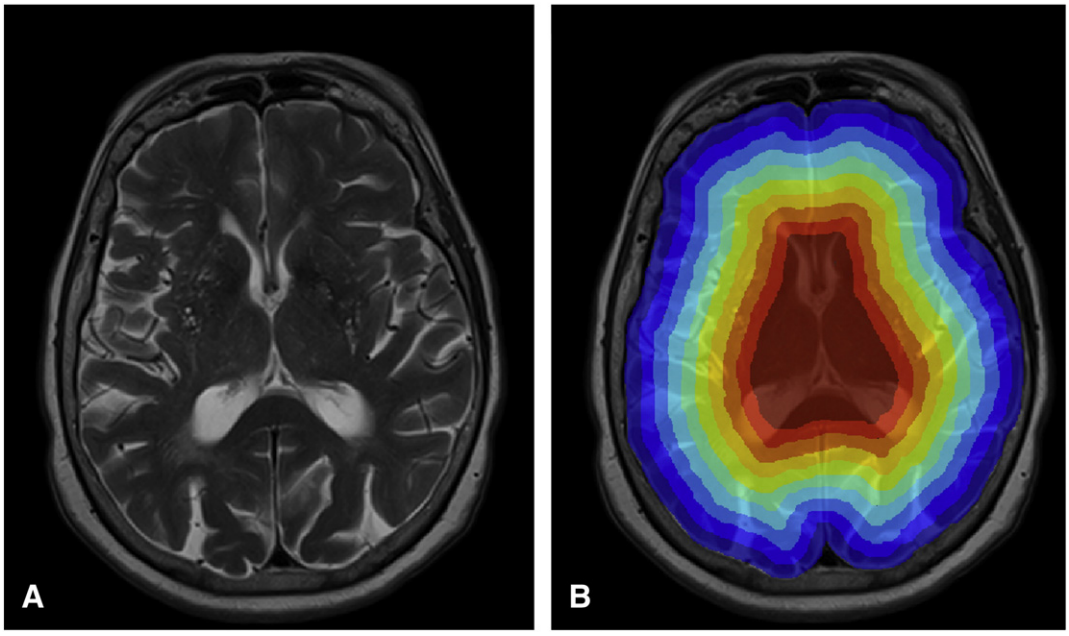

Fig. 3. (A) Transaxial T2w MR image traversing the central basal ganglia and (B) representation of the homeomorphic ROI's extending from the cortex to the center of the image plane.

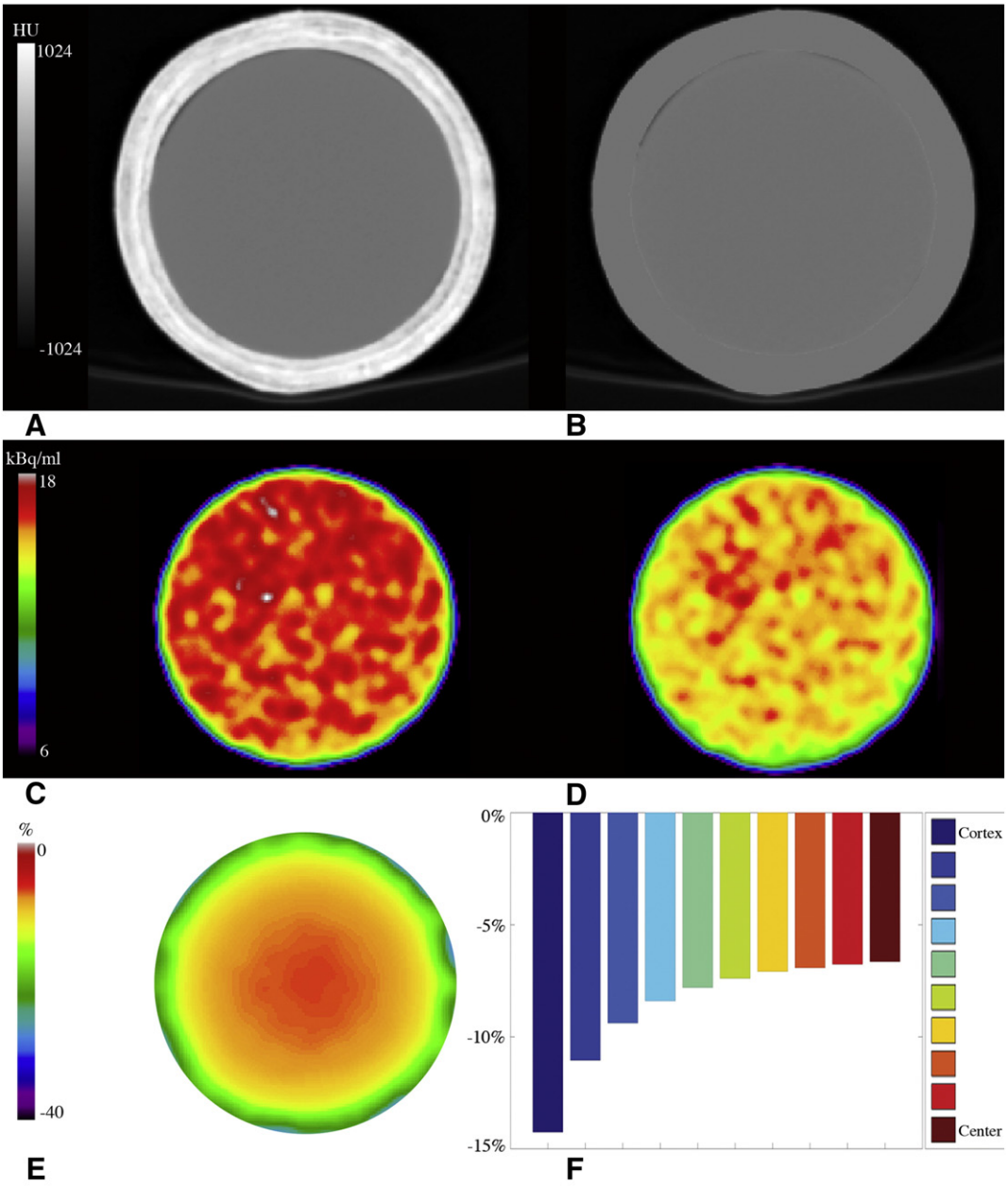

Fig. 4. Skull-type phantom: (A) transaxial image planes through the original CT, (B) segmented CT with plaster ("bone") values set to brain tissue, simulating DWFS MR-AC, (C, D) corresponding PET images after CT-AC using the image information in (A) and (B), (E) difference (Δ%) of the PET image values in (D) relative to (C), and (F) relative difference (Δ%) in the annulus ROI from Fig. 2C averaged across transverse image planes using the color coding from Fig. 2C.

essentially removed when adding bone from CT to the MR-AC map (MR_Bone, Fig. 8B) or when using the full CT for AC (MR_FullCT, Fig. 8C). The improvements from doing PET_{MR_Bone} or PET_{MR_FullCT} over PET_{MR_DWFS} are illustrated in Figs. 8D and E, respectively, involving only PET-data from PET/MR without being affected by physiological changes. In both cases there are improvements in all ROIs. The improvement increases monotonically towards the skull, from ~4% (center) to ~17% (cortex) for MR_Bone and from ~6% (center) to ~27% (cortex) for MR_FullCT.

Discussion

This study was motivated by observations of differences in the cortical activity distribution post [^{18}F]FDG injection of patients with suspected dementia undergoing combined PET/MR imaging at our institution. FDG-PET images of the brain from combined PET/MR showed a marked difference in the decay-corrected tracer activity distribution when compared to corresponding PET images from the single-injection FDG-PET/CT following standard CT-AC (Andersen et al., 2012). This is exemplified in Fig. 5. Therefore, we hypothesized that not accounting for bone tissue during standard MR-AC causes the reconstructed PET activity distribution in PET/MR to be biased (Fig. 1).

Our study is based on the acquisition of phantom and patient data using a fully-integrated PET/MR system with an implemented 4-tissue class DWFS MR-AC (Martinez-Möller et al., 2009).

Our simplified "skull" phantom was filled with a uniform activity concentration in water, and wrapped with layers of plaster, thus, mimicking a simplified 2D-brain phantom including the skull (Fig. 2). We observed a reduction of the mean activity values in the radial direction towards the skull in the transaxial PET/CT images following simulated MR-AC without considering bone attenuation values. The 7% difference in the central annulus region is also visually noticeable (Figs. 4C and D). The measured

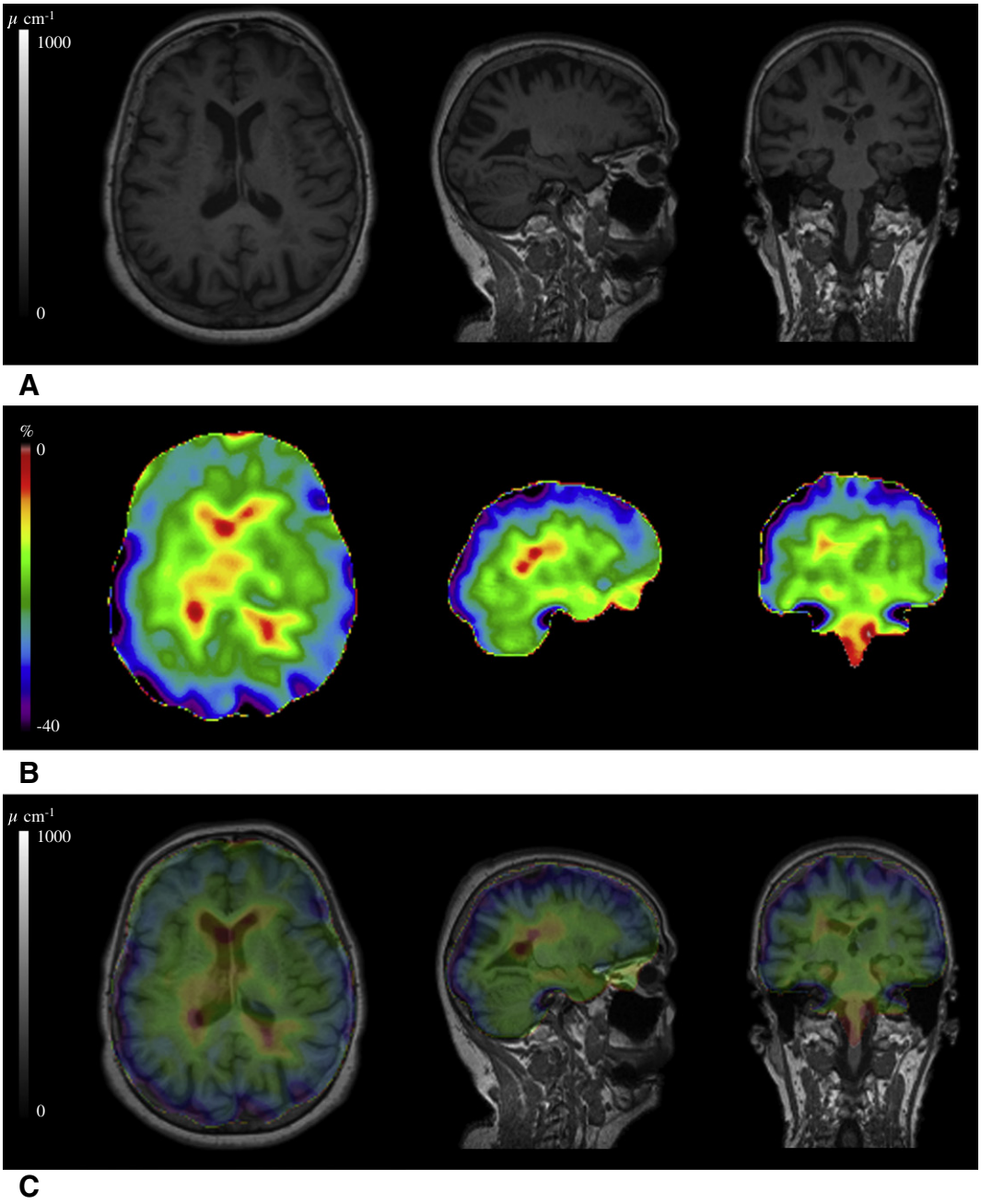

Fig. 5. Example PET/MR study of patient 10 (Table 1) following DWFS MR-AC: (A) T1w MR, (B) relative %-difference $\Delta\%(PET_{MR\_DWFS}, PET_{CT})$ and (C) PET_{MR_DWFS}/MR fusion overlay.

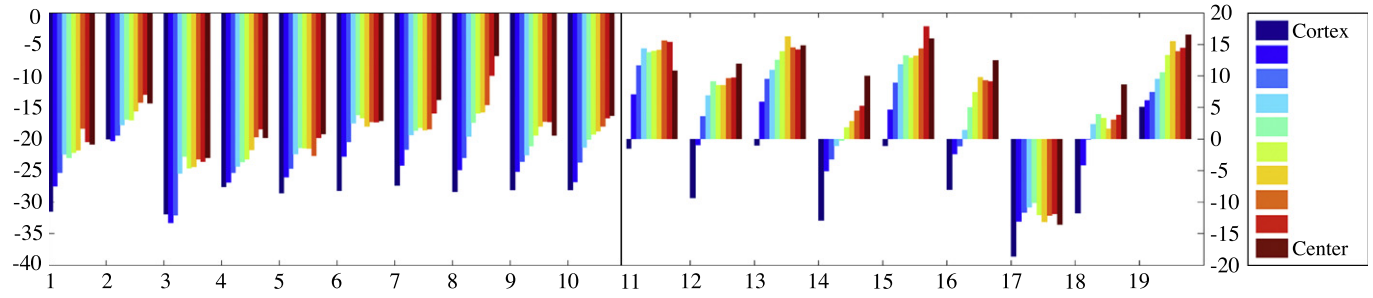

Fig. 6. Plots of subject-specific relative %-differences, $\Delta\%(PET_{MR\_DWFS}, PET_{CT})$ of reconstructed mean PET activity concentrations in the homeomorphic regions (Fig. 3). Separation is provided for subjects undergoing PET/MR prior to PET/CT (left panel) and those undergoing scans in reverse order (right panel). Note, differences are plotted on the same absolute scale (max. 40%) except that the zero-crossing was shifted for visibility in the right panel. Patient 3, 8, 12 and 17 had severe artifact in the DWFS attenuation map due to the presence of dental implants (Table 1).

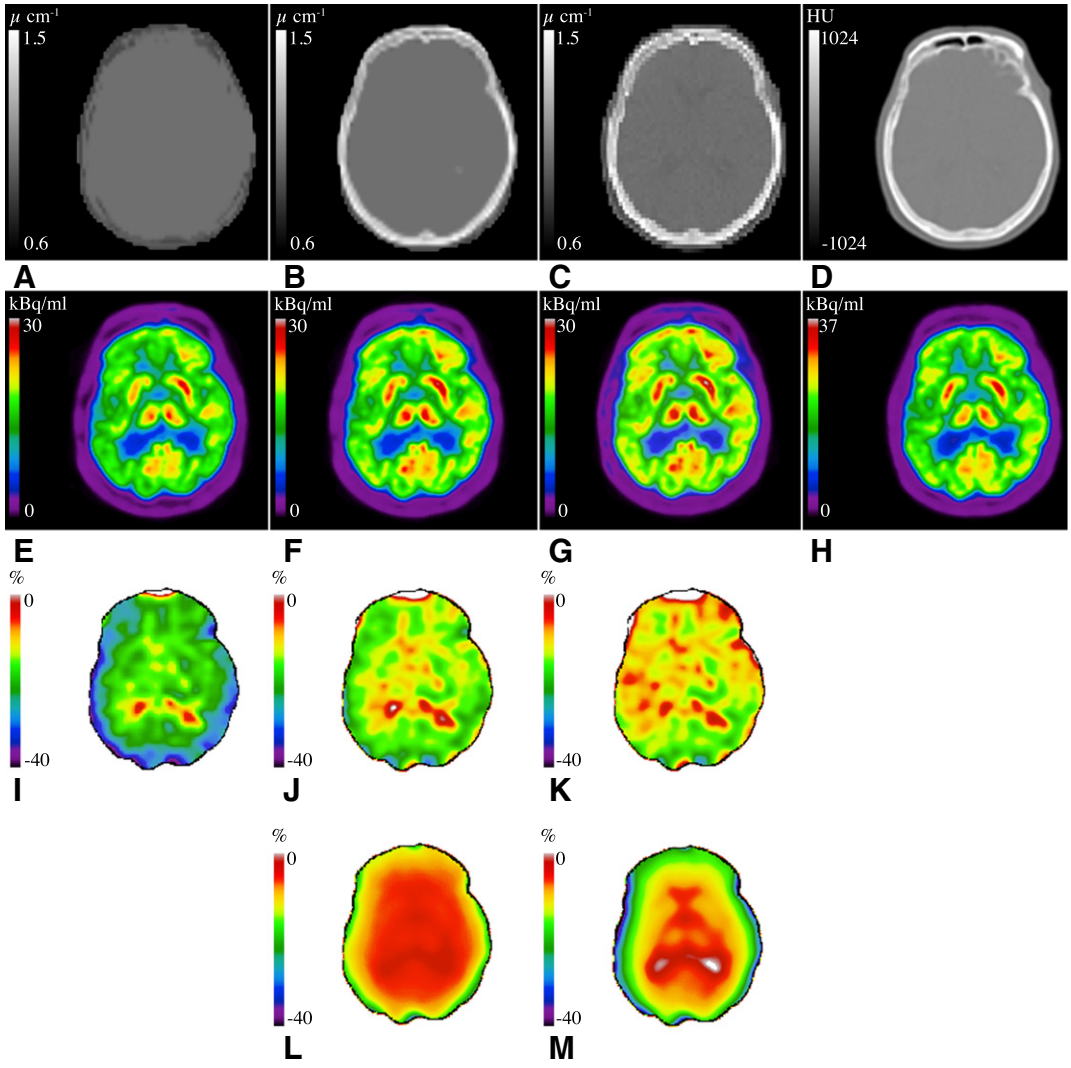

Fig. 7. Case study (patient 10, Table 1) with set of transaxial image planes: (A) original MR attenuation map (MR_DWFS), (B) MR attenuation map with superimposed bone attenuation values (MR_Bone), (C) MR replaced with co-registered full CT (MR_FullCT) and (D) original CT (CT). Image planes (E–H) represent the corresponding PET images reconstructed following AC using the attenuation information in (A–D). The scale in (H) was adapted to account for the change in tracer distribution from the elapsed time between the scans. Δ%-images with respect to PET_{CT} are shown for PET_{MR_DWFS} (I), PET_{MR_Bone} (J) and PET_{MR_FullCT} (K) demonstrating a markedly reduced gradient effect in (J) and (K). Panels (L) and (M), respectively, show the relative %-difference image of (F) and (G) with respect to PET_{MR_DWFS} (E).

values are fully compatible with the illustration in Fig. 1 in that the problem is caused by the differential average path length through bone structures for photons originating at the center and at the edge. The argument can easily be transferred from the 2D cylinder to a 3D sphere, and to the brain. Both, the visual and quantitative observations from the phantom study are replicated in our clinical patient population that included 19 patients with dementia. PET/MR images following DWFS MR-AC (PET_{MR_DWFS}) showed lower PET signal in cranio-lateral cortical regions of the brain relative to the central regions when compared to PET_{CT}. This is consistent for all 19 patients (Fig. 6). The observed shift (30%) of the relative difference of PET/MR and PET/CT images is attributed to the reverse scan order in the two patient groups (Table 1) and the continuous uptake of [^{18}F]FDG during the intermittent time between scans. The FDG uptake in brain tissue is well described from dynamic studies. It continues to increase for about 2 h, but with steadily decreasing slope as the maximum is approached (Hasselbalch et al., 1999; Spence et al., 2004). Therefore, the difference of FDG uptake between two time points does not only depend on the time difference, but also on the absolute time after injection. In our study, the two differences presumably are of about the same magnitude, since for the group with the longer of the two intervals, the first scan is also started later.

Fig. 8 summarizes the mean differences in AC-PET following standard and modified AC across subjects without dental artifacts. Using state-of-the-art PET/MR imaging and implementations of MR-AC we found an average bias of 10–15 percentage points between center and cortex (Fig. 8A) of the PET activity concentration relative to PET/CT in a sample axial slice through the basal ganglia. This bias may vary with the density, thickness and curvature of the cortical bone structures (Catana et al., 2012).

When bone attenuation was accounted for (MR_Bone and MR_FullCT) the gradient effect of the reconstructed PET activity distribution was removed with the mean relative %-differences being the same across all ROIs (Figs. 8B and C). For MR_Bone AC the relative %-difference is around −15% or +15% for all homeomorphic ROIs depending on the scan order of PET/MR and PET/CT (Fig. 8B). The difference between the PET images following standard and MR_Bone attenuation correction (PET_{MR_DWFS} and PET_{MR_Bone}) represents a smooth function of the distance from the skull with a maximum difference in the cortical region of −17% (Fig. 8D). When replacing the MR-based attenuation map with the co-registered CT-based attenuation map including bone, soft tissue and intermediate values, as calculated from standard CT-AC (Carney et al., 2006), the relative %-difference between the PET/MR

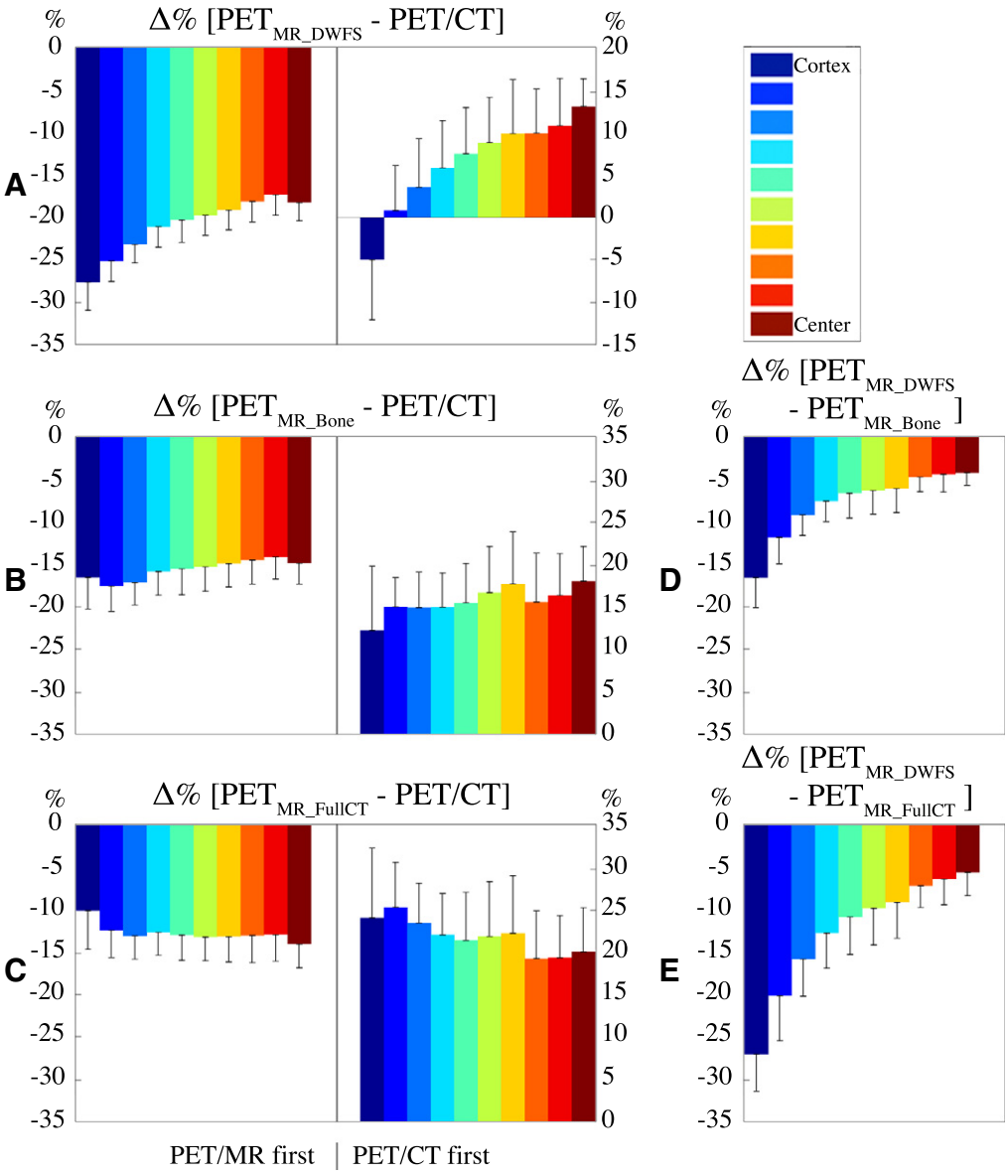

Fig. 8. Relative %-difference values for each of the homeomorphic ROI's averaged across all included patients. Difference values are shown relative to PET/CT for: (A) standard PET/MR — (PET_{MR_DWFS}), (B) PET/MR with superimposed bone attenuation map — (PET_{MR_Bone}) and (C) PET/MR with full CT-based attenuation map — PET_{MR_FullCT}. The difference values in panels (D) and (E) show directly the effect of applying MR_Bone and MR_FullCT compared to MR_DWFS. The values in (D) and (E) correspond well to the differences in (A–B and A–C). Note, the observed absolute difference between two groups is the result of both the physiological uptake (sign reversed with scan order) and a bias (not reversed) from the different corrections performed. Patient 1 (Table 1) was excluded from inclusion in C and E due to loss of data for PET reconstruction.

images and the original PET/CT images is also fairly uniform across the ROIs (Fig. 8C).

Although adding bone to the DWFS attenuation map removes the observed radial differences in the PET/MR images, we observed a residual difference of AC-PET values of 10%, or less between PET_{MR_Bone} and PET_{MR_FullCT} (Figs. 8B, C). This difference may be caused by two effects. Firstly, the implementation of the DWFS attributes a constant value of 0.100 cm^{-1} to soft tissue, while the CT-based attenuation values inside the skull are slightly lower (0.0974 cm^{-1}) and regionally variable. Secondly, the full_CT attenuation map is slightly larger than the DWFS-map, adding a few mm of soft tissue around the skull which more than compensates the lower values inside. The overall result is a larger attenuation correction, weighted towards the edge, cf. Fig. 8D versus Fig. 8E.

This study demonstrates the significance of the resulting underestimation of attenuation in PET/MR imaging of the brain using a standard 4-class segmentation method (Martinez-Möller et al., 2009). Both, phantom and clinical data illustrate a bias of attenuation-corrected and reconstructed PET activity concentrations. More importantly, this bias is spatially variable with a gradient pointing from the skull towards the center of the brain, most prominently seen on transaxial PET images traversing the central brain, but equally important in coronal and sagittal views (Fig. 5).

These findings are also confirmed by Hitz et al (Hitz et al., 2012) in a study of 32 patients with suspected dementia undergoing head-to-head comparisons of single-injection [^{18}F]FDG-PET/CT and -PET/MRI (Hitz et al., in review). Specifically, a voxel-based analysis revealed consistently lower tracer signal in PET/MR images following DWFS MR-AC in the cranio-lateral neocortex relative to the center, a finding that is in agreement with our results (Figs. 6 and 8). Hitz and co-workers further demonstrated a subsequent difference in observer-based rating of the PET/CT and PET/MR data in 20% of their patients. This illustrates a clinical significance of the spatially variable bias of attenuation corrected PET activity in standard PET/MR.

At the base of the skull an effect of not accounting for bone is also observed (see Fig. 5), but here the shape of the bone is more irregular, and the bone layer is often quite thin. Therefore, we do not see the same general radial decrease of reconstructed activity near the base of the brain, as we do close to the skull in the transaxial planes. Furthermore, MR susceptibility artifacts add another level of complexity to MR-based attenuation correction at the skull base. Addressing this issue falls outside the scope of this paper.

It is important to acknowledge that accurate quantification is essential to the clinical application of PET in the brain. Over the past decades a concerted effort has collected data of the clinical impact of PET brain imaging of a high quality enough to obtain FDA approval. This includes FDG (Silverman, 2004) and [^{18}F]Florbetapir (Clark et al., 2012) for the use in dementia correlated with autopsy data. There are several other [^{18}F]-labeled tracers targeting amyloid in the brain, that are in the process of being approved. Further, a large multicenter study, the Alzheimer's Disease Neuroimaging Initiative (ADNI), has been funded to define the progression of Alzheimer's disease though biomarkers for the purpose of scientific investigation, teaching or planning clinical research studies. For primary brain tumors threshold values have been meticulously established through multiple biopsies to best identify and define boundaries of primary brain tumors using e.g. [^{18}F]Fluoro-Ethyl-Tyrosin (FET) (Pauleit et al., 2005) for planning preoperatively or for radiation therapy. All of the above applications are dependent on the ability to accurately quantify the tracer concentration in tissue.

The brain imaging data acquired with the present state of combined PET/MR technology is likely to fail the site qualification necessary to be accepted in multicenter studies such as ADNI and for the clinical trials running using brain amyloid modifying agents (Ostrowitzki et al., 2011). Furthermore, accurate neuroreceptor quantification will not be possible, whether it is based on absolute measurement or applies a reference tissue model, typically with cerebellum as the reference.

In order to address the needs for absolute quantification laid out above, alternative strategies towards AC for brain studies are required. A number of approaches have been proposed that include machine learning algorithms in combination with an atlas database, bone segmentation based on ultra-short echo time (UTE) MR imaging as well as special image reconstruction algorithms that estimate, both, the emission activity and the attenuation from the PET emission data (Bezrukov et al., 2013).

Limitations

Our study has several limitations. Firstly, we simulated bone tissue by plaster, which has a slightly lower density than cortical bone. Therefore, the numerical results from the phantom and the patient study cannot be compared directly. Secondly, a similar intra-scan delay in the two patient groups was challenged by logistics issues during routine clinical operation of PET/CT and PET/MR in our department. Thirdly, our original subject population was reduced by drop-outs caused by severe dental artifacts in PET/MR, which could not be corrected for in view of a lack of retrospective correction algorithms for dental work. Fourthly, our data analysis approach is best suited for quantification of the global radial gradients manifest with DWFS MR-AC. In attenuation correction strategies using UTE where regional aberrations may predominate a data driven approach may be more appropriate (Catana et al., 2010).

Conclusion

Accurate attenuation correction is needed to achieve quantitative PET images. Failure to account for bone attenuation during standard MR-based attenuation correction of PET/MR data introduces a significant bias in the area of the cortex as compared to PET/CT following standard CT-AC. Of note, this bias is spatially variable being highest in the outer cortical structures and lower in the central brain. The effect can be understood from simple first principles of PET imaging and correction. Both absolute differences and regional variations can be markedly reduced when accounting for bone attenuation as part of the MR-AC. Therefore, refinements to existing MR-AC methods, or alternative strategies need to be found prior to adopting PET/MR imaging of the brain in clinical routine and research.

Acknowledgments

The PET/MR system at Rigshospitalet was kindly provided by the John and Birthe Meyer Foundation, Denmark.

Conflict of interest

TB is founder and employee of cmi-experts GmbH and reports no conflict with this manuscript.

References

Andersen, F.L., Keller, S.H., Hansen, A.E., Beyer, T., Law, I., Højgaard, L., Holm, S., 2012. Bone attenuation in brain-PET/MR imaging should be accounted for during attenuation correction and PET reconstruction. Eur. J. Nucl. Med. Mol. Imaging 39 (2), 174.

Beyer, T., Freudenberg, L.S., Czernin, J., Townsend, D.W., 2011. The future of hybrid imaging-part 3: PET/MR, small-animal imaging and beyond. Insights Imaging 2 (3), 235–246.

Bezrukov, I., Mantlik, F., Schmidt, H., Schölkopf, B., Pichler, B.J., 2013. MR-based PET attenuation correction for PET/MR imaging. Semin. Nucl. Med. 43 (1), 45–59.

Budinger, T.F., 1983. Time-of-flight positron emission tomography: status relative to conventional PET. J. Nucl. Med. 24 (1), 73–78.

Burger, C., Goerres, G., Schoenes, S., Buck, A., Lonn, A.H., Von Schulthess, G.K., 2002. PET attenuation coefficients from CT images: experimental evaluation of the transformation of CT into PET 511-keV attenuation coefficients. Eur. J. Nucl. Med. Mol. Imaging 29 (7), 922–927.

Carney, J.P., Townsend, D.W., Rappoport, V., Bendriem, B., 2006. Method for transforming CT images for attenuation correction in PET/CT imaging. Med. Phys. 33 (4), 976–983.

Catana, C., van der Kouwe, A., Benner, T., Michel, C.J., Hamm, M., Fenchel, M., Fischl, B., Rosen, B., Schmand, M., Sorensen, A.G., 2010. Towards implementing an MRI-based PET attenuation–correction method for neurologic studies on the MR–PET brain prototype. J. Nucl. Med. 51 (9), 1431–1438.

Catana, C., Drzezga, A., Heiss, W.D., Rosen, B.R., 2012. PET/MRI for neurologic applications. J. Nucl. Med. 53 (12), 1916–1925.

Clark, C.M., Pontecorvo, M.J., Beach, T.G., Bedell, B.J., Coleman, R.E., Doraiswamy, P.M., Fleisher, A.S., Reiman, E.M., Sabbagh, M.N., Sadowsky, C.H., Schneider, J.A., Arora, A., Carpenter, A.P., Flitter, M.L., Joshi, A.D., Krautkramer, M.J., Lu, M., Mintun, M.A., Skovronsky, D.M., AV-45–A16 Study Group, 2012. Cerebral PET with florbetapir compared with neuropathology at autopsy for detection of neuritic amyloid-β plaques: a prospective cohort study. Lancet Neurol. 11 (8), 669–678.

Delso, G., Fürst, S., Jakoby, B., Ladebeck, R., Ganter, C., Nekolla, S.G., Schwaiger, M., Ziegler, S.I., 2011. Performance measurements of the Siemens mMR integrated whole-body PET/MR scanner. J. Nucl. Med. 52, 1914–1922.

Hasselbalch, S.G., Knudsen, G.M., Videbaek, C., Pinborg, L.H., Schmidt, J.F., Holm, S., Paulson, O.B., 1999. No effect of insulin on glucose blood–brain barrier transport and cerebral metabolism in humans. Diabetes 48 (10), 1915–1921.

Heiss, W.D., 2009. The potential of PET/MR for brain imaging. Eur. J. Nucl. Med. Mol. Imaging 36 (1), 105–112.

Hitz, S., Habekost, C., Delso, G., Souvatzoglou, M., Grimmer, T., Beer, A., Fürst, S., Ziegler, S., Schwaiger, M., Drzezga, A., 2012. Evaluation of the qualitative performance of PET/MR versus PET/CT in patients with Alzheimer's disease. J. Nucl. Med. 53 (1), 1932.

Hitz, S., Habekost, C., Fürst, S., Delso, G., Föster, S., Ziegler, S., Nekolla, G., Souvatzoglou, M., Beer, A., Grimmer, T., Schwaiger, M., Drzezga, A., 2013w. Qualitative performance of an integrated whole-body PET/MR scanner for brain imaging: systematic comparison to conventional PET/CT inpatients examined for suspected dementia with [18F]FDG. J. Nucl. Med. (in review).

Hofmann, M., Pichler, B., Schölkopf, B., Beyer, T., 2009. Towards quantitative PET/MRI: a review of MR-based attenuation correction techniques. Eur. J. Nucl. Med. Mol. Imaging 39 (1), 93–104.

Huang, S.C., Hoffman, E.J., Phelps, M.E., Kuhl, D.E., 1979. Quantitation in positron emission computed tomography: 2. Effects of inaccurate attenuation correction. J. Comput. Assist. Tomogr. 3 (6), 804–814.

Jakoby, B.W., Bercier, Y., Conti, M., Casey, M.E., Bendriem, B., Townsend, D.W., 2011. Physical and clinical performance of the mCT time-of-flight PET/CT scanner. Phys. Med. Biol. 56 (8), 2375–2389.

Kalemis, A., Delattre, B.M., Heinzer, S., 2013. Sequential whole-body PET/MR scanner: concept, clinical use, and optimisation after two years in the clinic. The manufacturer's perspective. MAGMA 26 (1), 5–23.

Keereman, V., Mollet, P., Berker, Y., Schulz, V., Vandenberghe, S., 2013. Challenges and current methods for attenuation correction in PET/MR. MAGMA 26 (1), 81–98.

Keller, S.H., Holm, S., Hansen, A.E., Sattler, B., Andersen, F., Klausen, T.L., Højgaard, L., Kjær, A., Beyer, T., 2013. Image artifacts from MR-based attenuation correction in clinical, whole-body PET/MRI. MAGMA 26 (1), 173–181.

Kinahan, P.E., Townsend, D.W., Beyer, T., Sashin, D., 1998. Attenuation correction for a combined 3D PET/CT scanner. Med. Phys. 25, 2046–2053.

Krak, N.C., van der Hoeven, J.J., Hoekstra, O.S., Twisk, J.W., van der Wall, E., Lammertsma, A.A., 2003. Measuring [(18)F]FDG uptake in breast cancer during chemotherapy: comparison of analytical methods. Eur. J. Nucl. Med. Mol. Imaging 30 (5), 674–681.

LaCroix, K.J., Tsui, B.M.W., Hasegawa, B.H., Brown, J.K., 1994. Investigation of the use of X-ray CT images for attenuation compensation in SPECT. IEEE Trans. Nucl. Sci. 41 (6), 2793–2799.

Martinez-Möller, A., Souvatzoglou, M., Delso, G., Bundschuh, R.A., Chefd'hotel, C., Ziegler, S.I., Navab, N., Schwaiger, M., Nekolla, S.G., 2009. Tissue classification as a potential approach for attenuation correction in whole-body PET/MRI: evaluation with PET/CT data. J. Nucl. Med. 50, 520–526.

Ostrowitzki, S., Deptula, D., Thurfjell, L., et al., 2011. Mechanism of amyloid removal in patients with Alzheimer disease treated with gantenerumab. Arch. Neurol. 69 (2), 198–207.

Pauleit, D., Floeth, F., Hamacher, K., et al., 2005. O-(2-[18F]fluoroethyl)-L-tyrosine PET combined with MRI improves the diagnostic assessment of cerebral gliomas. Brain 128, 678–687.

Pichler, B.J., Kolb, A., Nägele, T., Schlemmer, H.P., 2010. PET/MRI: paving the way for the next generation of clinical multimodality imaging applications. J. Nucl. Med. 51 (3), 333–336.

Schulz, V., Torres-Espallardo, I., Renisch, S., Hu, Z., Ojha, N., Börnert, P., Perkuhn, M., Niendorf, T., Schäfer, W.M., Brockmann, H., Krohn, T., Buhl, A., Günther, R.W., Mottaghy, F.M., Krombach, G.A., 2011. Automatic, three-segment, MR-based attenuation correction for whole-body PET/MR data. Eur. J. Nucl. Med. Mol. Imaging 38, 138–152.

Silverman, D.H., 2004. Brain 18FFDG PET in the diagnosis of neurodegenerative dementias: comparison with perfusion SPECT and with clinical evaluations lacking nuclear imaging. J. Nucl. Med. 45 (4), 594–607.

Spence, A.M., Muzi, M., Mankoff, D.A., O'Sullivan, S.F., Link, J.M., Lewellen, T.K., Lewellen, B., Pham, P., Minoshima, S., Swanson, K., Krohn, K.A., 2004. 18F-FDG PET of gliomas at delayed intervals: improved distinction between tumor and normal gray matter. J. Nucl. Med. 45 (10), 1653–1659.

Wagenknecht, G., Kaiser, H.J., Mottaghy, F.M., Herzog, H., 2013. MRI for attenuation correction in PET: methods and challenges. MAGMA 26 (1), 99–113.

Wahl, R.L., Quint, L.E., Cieslak, R.D., Aisen, A.M., Koeppe, R.A., Meyer, C.R., 1993. "Anatometabolic" tumor imaging: fusion of FDG PET with CT or MRI to localize foci of increased activity. J. Nucl. Med. 34 (7), 1190–1197.

Watson, C.C., 1997. A technique for measuring the energy response of a PET tomograph using a compact scattering source. IEEE Trans. Nucl. Sci. 44 (6), 2500–2508.

Zaidi, H., Ojha, N., Morich, M., Griesmer, J., Hu, Z., Maniawski, P., Ratib, O., Izquierdo-Garcia, D., Fayad, Z., Shao, L., 2011. Design and performance evaluation of a whole-body ingenuity TF PET–MRI system. Phys. Med. Biol. 56, 3091–3106.